Surface texture modulation via buckling in porous inclined mechanical metamaterials

Matheus C. Fernandes [a,b,1], Saurabh Mhatre [c,1], Antonio E. Forte [a,d,e], Bing Zhao [a,f], Olga Mesa [c,g], James C. Weaver [a,b], Martin Bechthold [c], Katia Bertoldi [a,b,*]

[a] John A. Paulson School of Engineering and Applied Sciences, Harvard University, Cambridge, MA 02138, United States of America
[b] Wyss Institute, Harvard University, Cambridge, MA 02138, United States of America
[c] Graduate School of Design, Harvard University, Cambridge, MA 02138, United States of America
[d] Department of Electronics, Information and Bioengineering, Politecnico di Milano, Milan, 20133, Italy
[e] Department of Engineering, King's College London, London, WC2R 2LS, UK
[f] Space Structures Research Center, Shanghai Jiao Tong University, Shanghai 200240, China
[g] School of Architecture, Roger Williams University, Bristol, RI 02809, UK

ARTICLE INFO

ABSTRACT

Porous materials with well-defined periodicity are commonly encountered in biological and synthetic structures and exhibit a wide range of behaviors, ranging from negative Poisson's ratios, to high energy absorption and acoustic damping. Recently, the response of these systems has been shown to be enhanced by mechanical instabilities that lead to sudden and reversible geometric transformations. Although buckling induces planar transformations in most of 2D porous metamaterials, here we describe the emergence of 3D morphologies triggered by mechanical instabilities in an elastomeric block with tilted cylindrical holes. As a proof of concept, we demonstrate that these structures can be leveraged to tune surface properties including friction and light reflection, thus providing a new experimental platform for investigating deformation-dependent dynamics for tribological and optical applications.

1. Introduction

Recently, instabilities have been recognized as a feature to be harnessed rather than avoided [1]. For example, mechanical metamaterials can be designed to trigger instabilities upon loading, which can lead to dramatic changes in geometry and create functionality [2–4]. Among numerous designs, one of the simplest is a block of elastomer with a square array of cylindrical holes [5–7]. When this structure is compressed in the plane perpendicular to the long axis of the holes, the beam-like ligaments separating them buckle cooperatively. Such instabilities lead to a sudden transformation of the circular holes into mutually orthogonal ellipses. This reversible morphological change has been harnessed to realize structures with unusual mechanical properties, such as negative Poisson's ratio [8] and negative swelling ratio [9], which can function as phononic and photonic switches [10–14], color displays [14], and soft robots capable of grasping and walking [15].

While the geometric transformations induced by buckling in 2D porous metamaterials are typically planar, buckling can also trigger the formation of out-of-plane 3D patterns. For example, a bilayer system comprising a thin elastic film covering a pre-strained soft substrate can undergo a buckling instability, leading to the formation of complex wrinkle patterns [16,17]. These wrinkles have been investigated for applications ranging from stretchable electronics [18,19] and diffraction gratings [17, 20], to reversibly adhesive pads [21] and tunable flow control in microfluidic devices [22]. Beyond these bilayer systems, mechanical instabilities in kirigami sheets can also result in out-of-plane deformations that have been exploited to realize morphable structures [23–26] or the skin of snake-inspired crawling actuators [27].

Here, inspired by a tilted cuboid structure that can fold into a 3D configuration [28], we show that buckling generates complex 3D morphologies in a new porous metamaterial comprising a square array of tilted cylindrical holes within an elastomeric matrix. We demonstrate that such buckling-induced 3D deformations can be harnessed to actively control surface properties such as reflectance and friction, providing new opportunities for the production of tunable light-diffusion devices and crawling robots. Finally, we show that this concept can be extended to different

---

* Correspondence to: Attn: Prof. Katia Bertoldi, 29 Oxford St, Cambridge MA, 02138, United States of America.
E-mail address: bertoldi@seas.harvard.edu (K. Bertoldi).
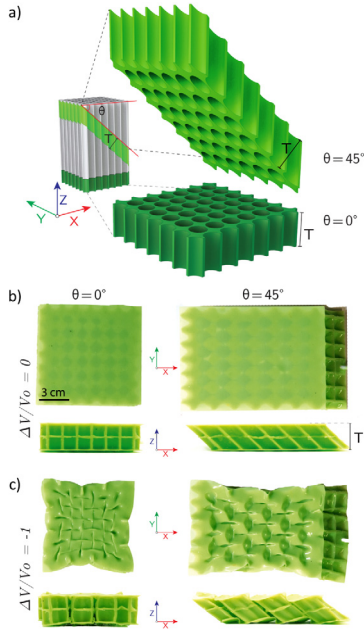[1] Equal contribution authors.

Fig. 1. Conceptual visualization and buckling-induced geometric transformations in our inclined metamaterial. (a) Shown in light green, this structure is derived from conceptually slicing a block (shown in gray), containing a square array of cylindrical holes, at an angle θ. (b)–(c) pre- and post-buckling photos of the metamaterial at (b) $\Delta V/V_0 = 0$ and at (c) $\Delta V/V_0 = -1$ configurations for samples with $\theta = 0°$ (left) and $\theta = 45°$ (right). Both top and side views are shown. Additional information on this figure can be found in Supplementary Video 1. (For interpretation of the references to color in this figure legend, the reader is referred to the web version of this article.)

Fig. 2. Experimental characterization of out-of-plane metamaterial buckling. (a) Pressure–volume relationship for the four different θ's considered (θ=0°, 15°, 30°, 45°). Each sample was tested independently three times and the results from each test are reported as separate lines. (b) Normalized out-of-plane deformation measurements of the samples, obtained from 3D surface scans. The inset specifies the four regions (denoted by white boxes) used for measuring δ. Additional information on this figure can be found in Supplementary Video 2. (For interpretation of the references to color in this figure legend, the reader is referred to the web version of this article.)

periodic arrangements of tilted cylindrical holes, thus providing a new platform to control surface morphology in flexible structures, along with innovative design rules for the production of smart surfaces, soft robots, and active facades for architectural applications.

2. Metamaterial architecture

In this study, we investigate a metamaterial conceptually obtained from slicing a block of elastomer, containing a square array of cylindrical holes aligned along the z-axis, at an angle θ with respect to the xy-plane (Fig. 1(a)). The holes in the gray starting block have a radius $R_h = 5.83$ mm and center-to-center distance d_h, chosen so that the initial porosity is $\phi_0 = \pi R_h^2/d_h^2 = 0.59$, which provides the structure a large enough hinge thickness to balance the structure's stiffness and out-of-plane displacement. The resulting metamaterial has an out-of-plane thickness $T = 23.32$ mm and elliptical holes on its top and bottom faces (Fig. 1(a)) with major and minor axis of length $R_h/\cos\theta$ and R_h, respectively.

3. Out-of-plane deformation upon deflation

The structures were fabricated from a silicone elastomer (Zhermack Elite Double 32) utilizing a molding approach, and hydraulic actuation was employed to load the structures, while minimizing boundary effects. To achieve this behavior, the metamaterial was made air/water-tight by covering its top and bottom faces with thin elastomeric sheets (with thickness of ∼0.5 mm). A single pressure input actuation was achieved by connecting the cylindrical cavities via channels and slowly removing a ΔV volume of water through a syringe pump (see Supplementary Information
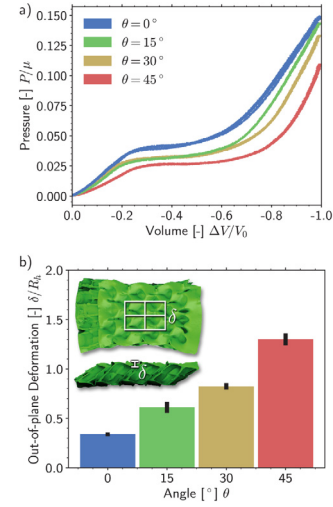
(SI) Section S1, S2 and S3, and Fig. S1–S3 for details on geometry, fabrication, and experimental testing).

In Fig. 1(b)–(c), we show photos of the metamaterial with $\theta = 0°$ and 45° for $\Delta V/V_0 = 0$ (initial configuration - Fig. 1(b)) and $\Delta V/V_0 = -1$ (Fig. 1(c)), where V_0 denotes the total volume of the holes in the initial (non-evacuated) configuration. As expected [15], in the negative pressure regime, the ligaments separating the cavities buckle cooperatively, triggering a sudden transformation of the circular holes into a periodic pattern of alternating, and mutually orthogonal, elliptical holes. For the structure with $\theta = 45°$, such transformations were accompanied by the formation of a periodic 3D pattern on its initially flat outer surfaces, suggesting that the angle θ may be exploited to trigger the formation of out-of-plane textured geometries.

To better understand the effect of θ on the post-buckling geometry of this class of metamaterials, we fabricated and characterized examples with $\theta = 0°$, 15°, 30° and 45°. The water-filled structures were connected to a syringe pump and the incompressible fluid was slowly removed from the cavities, while monitoring the evolution of the pressure using a pressure sensor (MPX5050DP, NXP USA Inc) (see SI Section 3.1 for details). The results reported in Fig. 2(a) demonstrate that all considered metamaterials are characterized by three distinct regions: (i) a linear elastic regime; (ii) a stress plateau following thereafter; and (iii) stiffening by further deflation. While in the initial linear regime the holes homogeneously contracted and the samples remained flat, the sudden departure from linearity to a plateau pressure was caused by the buckling of the ligaments. Remarkably, for $\theta \neq 0°$ the instability triggered the morphing of the sample's surfaces and produced 3D patterns with similar geometric features, whose sizes varied with θ (see SI Fig. S5 for more information).

To quantify the magnitude of the associated out-of-plane deformation, we used a hand-held 3D scanner (Artec Space Spider, Artec Studio 14.1.1.75) and recorded the buckled surface profile at $\Delta V/V_0 = -1$ (see SI Fig. S6 and SI Section S3.2 for more details). For these measurements, we focused on the four central unit cells of the sample (see dashed rectangles in Fig. 2(b) inset) and
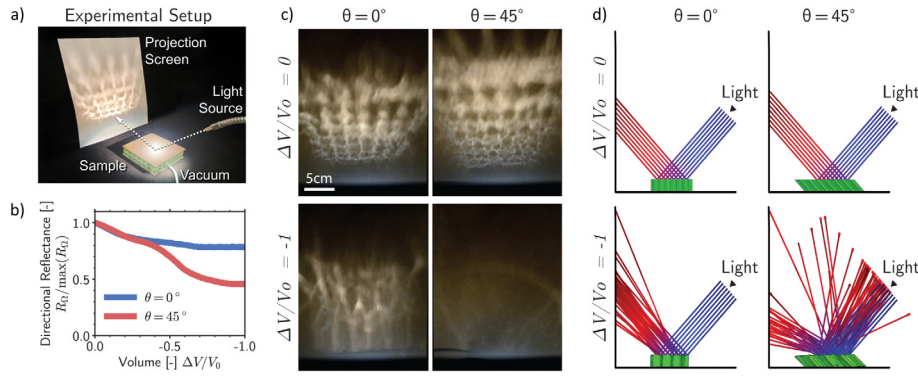
Fig. 3. Buckling-induced tunable light reflection. (a) Photograph of the experimental setup outlining the sample location, light source, and pattern collection screen. (b) Evolution of the measured directional reflectance R_Ω (normalized by $\max(R_\Omega)$) as a function of $\Delta V/V_0$ for samples with $\theta = 0°$ and $\theta = 45°$. (c) Snapshots obtained during the deflation process for the $\theta = 0°$ (left column) and $\theta = 45°$ (right column) samples at $\Delta V/V_0 = 0$ (top row) and $\Delta V/V_0 = -1$ (bottom row). (d) Ray tracing simulations showing the directionality of light reflection for $\theta = 0°$ (left column) and $\theta = 45°$ (right column) samples at $\Delta V/V_0 = 0$ (top row) and $\Delta V/V_0 = -1$ (bottom row). For reference, the initial periodic reflected light pattern is due to small surface depressions in the non-evacuated structure. Additional information on this figure can be found in Supplementary Video 3. (For interpretation of the references to color in this figure legend, the reader is referred to the web version of this article.)

used a custom Python script to segment and detect the amplitude of the out-of-plane displacement in each of the four regions, $\delta = \max(u_z) - \min(u_z)$. In Fig. 2(b) we report the average of the four measured values of δ for each metamaterial. These results clearly show that the out-of-plane deformation of the structures becomes more accentuated as θ increases from 0° to 45°.

Since the buckling-induced textures have identical morphologies, but an out-of-plane amplitude that monotonically increases with θ, in the following sections, we only consider the metamaterials with $\theta = 0°$ and $\theta = 45°$. These two configurations provide the maximum difference in 3D deformation, and therefore represent the best candidates for demonstrating how the buckling-induced textures can be leveraged to modulate additional functionalities of these metamaterials, such as light reflection and friction.

4. Tunable light reflectance

To investigate buckling-induced tunable light reflection of our metamaterial, we turned its surface into a mirror by mixing gold paint with the silicone elastomer used for casting the thin membranes that formed the top and bottom surfaces of the structure. For the experiments, which were conducted in a dark room, we positioned a goose-neck halogen lamb at a distance of 9.5 cm from the sample and at an incident angle of 45° relative to the metamaterial's surface (see SI Section S3.3 for details). While filled with water, we slowly evacuated the structure and monitored the light reflected onto a white panel positioned at a distance of 11 cm from the sample (see Fig. 3(a)). As shown in Fig. 3(c), while for $\Delta V/V_0 = 0$, the amount of light reflected is similar for both the samples with $\theta = 0°$ and $\theta = 45°$, at $\Delta V/V_0 = -1$ it is substantially lowered for the $\theta = 45°$ structure. To quantify this light scattering behavior, we converted the recorded projection screen images to gray-scale, and measured the brightness of all pixels in this region of interest (denoted by the dashed red rectangle in Fig. 3(a)) and calculated the directional reflectance R_Ω as the mean of these values (see SI Section S3.3 for details). The results shown in Fig. 3(b) indicate that for $\Delta V/V_0 = -1$ the normalized directional reflectance, $R_\Omega / \max(R_\Omega)$, for the $\theta = 45°$ structure is 32% lower than that for the $\theta = 0°$ structure. This stark difference in performance is due to the fact that upon buckling of the top surface of the $\theta = 45°$ metamaterial, the incident rays are scattered in multiple directions, such that only few of them reach the white panel. This phenomenon is also clearly visible in simulations conducted

using the Ray Tracing Module in COMSOL (see SI Section S4.2 for details). The numerical results reported in Fig. 3(d) show that (i) for $\Delta V/V_0 = 0$ (i.e. when the top surface is flat) the metamaterial acts as a planar mirror irrespective of θ and reflects all rays at 45° angle; (ii) for $\Delta V/V_0 = -1$ the $\theta = 0°$ sample, on average, still reflects the incidents rays at a 45° angle from the sample surface, with small deviations due to small and local perturbations of the surface smoothness; (iii) for $\Delta V/V_0 = -1$ the $\theta = 45°$ sample reflects the light rays at vastly different angles from the sample surface — resulting in a diffuse distribution of light reflected in multiple directions. While wrinkling patterns have been proposed to create microlenses with variable focal length [16, 29] and achieve dynamic changes in optical transmittance and diffraction patterns [30], our results show that buckling in porous metamaterials also provides opportunities to control the specular and diffuse optical scattering, opening avenues for tuning sunlight reflection in architectural applications or the encryption of messages and graphics that reversibly appear and disappear due to actuation [30].

5. Tunable frictional properties

Changes in surface morphology can also translate into changes in frictional properties of a structure, and to demonstrate this behavior, we placed our metamaterial on an acrylic plate, containing a layer of masking tape (Duck 240883) to reduce surface friction. The acrylic plate was then tilted, and the smallest tilting angle for which the sample began sliding, ϕ_{cr}, was recorded. From these measurements, we calculated the coefficient of static friction $\mu = \tan\phi_{cr}$ as a function of ΔV for each geometry. Since μ is determined by the interaction between the substrate (tape) and the surface of the metamaterial, we found that μ remains constant when varying $\Delta V/V_0$ and/or θ for each sample. For example, if we consider the sample with $\theta = 45°$ (see Fig. 4(a), first column), we observed that the structure has the same tilting angle ϕ_{cr} in both the initial and the buckled configuration (Fig. 4(b), first column) - a feature that is also observed for the sample with $\theta = 0°$ (see SI Fig. S8). As such, the friction coefficient is $\mu \approx 0.95$ for any $\Delta V/V_0$ (gold bars in Fig. 4(c)).

Beyond the ability of these metamaterials to generate large-scale out-of-plane surface geometries, this behavior also offers the opportunity to expose/retract a third material, leading to a tunable μ. For example, if we simply attach small acrylic spheres in the areas of the surface that retract during buckling (Fig. 4(a),
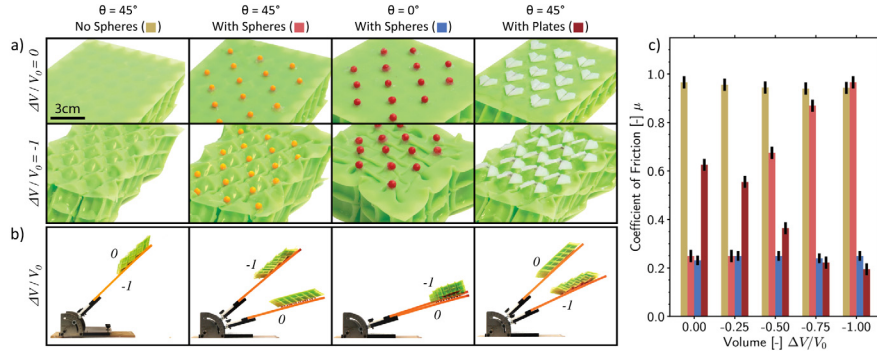
Fig. 4. Frictional measurements for our inclined metamaterial. (a) Photographs showing the bottom surface at the $\Delta V/V_0 = 0$ (top row) and $\Delta V/V_0 = -1$ (bottom row) states of samples with (from left to right): (i) $\theta = 45°$ and no acrylic features; (ii) $\theta = 45°$ and acrylic spheres; (iii) $\theta = 0°$ and acrylic spheres; (iv) $\theta = 45°$ and acrylic plates. (b) Photographs qualitatively showing the effect of the buckling-induced morphology on the tilting angle for which the sample began to slide, φ_{cr}. (c) Coefficient of friction for the different samples as a function of $\Delta V/V_0$. See SI Figs. S7-S9 for additional information and results. Additional information on this figure can be found in Supplementary Video 4. (For interpretation of the references to color in this figure legend, the reader is referred to the web version of this article.)

second column), such elements (i) dominate the contact properties in the initial configuration and (ii) disengage with the substrate under vacuum, which then comes in contact with the elastomer. This behavior enables switching from an acrylic-tape to a elastomer–tape interaction. As such, the frictional coefficient between the metamaterial and the substrate is low prior to buckling (with $\mu \approx 0.25$) and progressively increase as the buckling-induced pattern becomes more accentuated, eventually reaching $\mu \approx 0.95$ (pink bars in Fig. 4(c)). Note that in this structure, the changing in frictional behavior is solely due to the emergence of the 3D pattern induced through buckling. In fact, if we attach the same acrylic spheres to the surface of the sample with $\theta = 0°$, which does not exhibit a 3D pattern upon air evacuation (Fig. 4(a), third column), we find that $\mu \approx 0.25$ for both the initial and the buckled configuration (blue bars in Fig. 4(c)) as the spheres are always in contact with the substrate.

An effective friction coefficient μ that decrease as a function of $\Delta V/V_0$ is also achievable. By swapping the spheres with acrylic plates (Fig. 4(a), fourth column) coated by a thin layer of silicone adhesive (Sil-Poxy, Smooth-On), one can obtain a metamaterial with a friction coefficient that decrease upon air evacuation. Initially, the silicone adhesive is in contact with the substrate and $\mu \approx 0.62$. However, when the buckling-induced 3D pattern forms, the acrylic plates rotate and their edges (which are not coated) come in contact with the substrate, reducing μ to approximately 0.2 (dark red bars in Fig. 4(c)).

6. Soft crawling robot

To demonstrate this effect, we created a soft crawling robot that harnesses the switchable frictional properties of our metamaterial to achieve locomotion. The robot comprises three metamaterial modules (see Fig. 5(a)). The first module is characterized by $\theta = 45°$ and has spheres attached to its surface. The second module also has spheres attached to its surface, but with $\theta = 0°$. Finally, the third module ($\theta = 45°$) is rotated 180 degrees relative to the first, and contains acrylic plates instead of spheres. During assembly, the first and third modules of the robot were connected to the same pressure source, which allowed us to provide the same negative pressure at the front and the rear of the robot, and to reset it to atmospheric pressure, simultaneously. Moreover, in order to provide pressure continuity between the first and the second modules, we coupled these via a short tube (with 1.75 mm diameter).

In the initial configuration (photograph (i) in Fig. 5(b)) the friction coefficient between the first two modules and the substrate is $\mu \approx 0.25$, whereas for the third module, is $\mu \approx 0.6$.
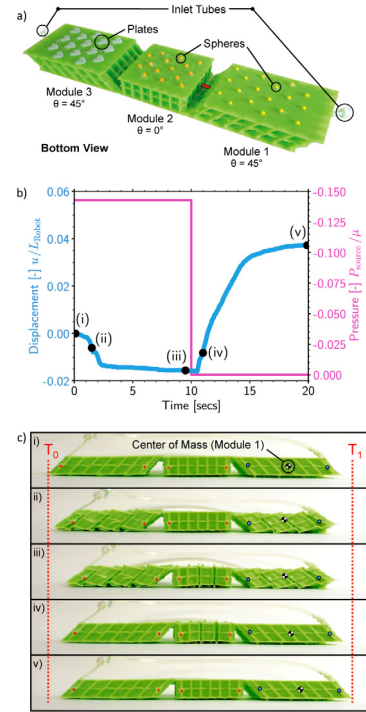

Fig. 5. Design elements and performance of our soft robotic crawler. (a) Photograph showing the bottom of the soft robotic crawler. (b) Displacement of the center of mass of the first module of the crawler, u, normalized by the initial length of the crawler, L_{robot}, (blue line) and source pressure, P_{source}, (magenta line) versus time during a cycle. The center of mass provides information on the average displacement of the first module of the robot, which is obtained by averaging the displacement of both edge points for each frame. (c) Experimental snapshots of our soft crawler at $t =$ (i) 0, (ii) 1.5, (iii) 9.5, (iv) 11 and (v) 20 s. The distance traveled during one full motion cycle (between T0 and T1) in indicated by the locations of the two red dotted lines. Additional information on this figure can be found in Supplementary Video 5. (For interpretation of the references to color in this figure legend, the reader is referred to the web version of this article.)

However, upon air evacuation, the coefficient of friction varies differently for each of the three modules (see Fig. 4(c)). Note that, for simplicity, in this demonstration we use a pressure controlled air vacuum line to power the robot, but the effect of fluid compressibility on the response of the system was negligible.

From analyzing the pressure–volume relationship reported in Fig. 2(a), we predict that the two modules with $\theta = 45°$ buckle

first, followed by the module with $\theta = 0°$, in the negative pressure regime. This sequence of events is confirmed through our experimental testing, which demonstrates that when a negative pressure pulse is provided to the robot (with magnitude $P_{source} = 50$ kPa for $t = 10$ s), we see that the first and third modules with $\theta = 45°$, which are connected to the same vacuum line, buckle before the second module with $\theta = 0°$ (snapshot (ii) in Fig. 5(b)). The emergence of the 3D pattern triggered by buckling leads to an increase in friction (from $\mu \approx 0.25$ to $\mu \approx 0.95$) for the first module, which becomes an anchoring point. At the same time, the third module loses its ability to grip (from $\mu \approx 0.6$ to $\mu \approx 0.2$), which facilitate its forward sliding. Finally, the second module buckles (snapshot (iii) in Fig. 5(b)). Since buckling only leads to its contraction but does not change its frictional properties, this module merely acts as an stroke amplifier and gets pulled forward. As a result, at the end of complete air evacuation the robot advances on average by 9.3 ± 0.4 mm (Fig. 5(c)).

In the second step of the gait cycle, we release the robot from the vacuum, by simultaneously opening the first and the third modules to the atmosphere. According to the pressure–volume relationship reported in Fig. 2(a) the second module (with $\theta = 0°$) should unbuckle first, followed by the $\theta = 45°$ samples. However, in our experiments the first and third modules (with $\theta = 45°$) unbuckle immediately (snapshot (iv) in Fig. 5(b)), due to their proximity to the outlets at atmospheric pressure. The relaxing of the 3D pattern on the surface of the first module removes the anchoring point, as the friction decreases from $\mu \approx 0.95$ to $\mu \approx 0.25$. At the same time, the third module regains grip, becoming the new anchoring point. Successively, when the middle module unbuckles (snapshot (v)) the robot slides forward again, advancing on average by additional 8.7 ± 0.4 mm (Fig. 5(c)). As a result, at the end of the complete gait cycle, the crawling robot advances on average by 18 mm (Fig. 5(c)).

7. Conclusion

To summarize, in the present work we investigated the properties of a metamaterial consisting of an elastomeric block with a square array of tilted cylindrical holes. We discovered that the hole tilting angle (θ) plays a major role in the out-of-plane buckling behavior and the emergence of 3D morphologies on the exposed surfaces of the samples. Furthermore, we demonstrated how these patterns can be utilized to control surface properties (including light reflectance and friction) by means of a simple hydraulic or pneumatic actuation.

Although throughout this study, we focused on a square array of holes, this concept can be also extended to different hole arrangements. To explore this avenue, we used Finite Element analyses to simulate metamaterials with different periodic distributions of cylindrical holes (more details of which can be found in SI Section S4.1). Specifically, we focused on arrangements that have been previously shown to reversibly switch between expanded (i.e. with circular holes) and compact (i.e. with elongated, almost fully closed elliptical holes) configurations for $\theta = 0°$ [31]. In full agreement with previous studies [31], we find that when the holes' axes are perpendicular to the top and bottom surfaces, buckling triggers a planar geometric transformation (see SI Fig S4). In contrast, as shown in SI Fig S10 and Supplementary Video 6, for $\theta = 45°$, all geometries exhibit different buckling-induced out-of-plane deformation patterns. These results suggest that our approach can be used to achieve more complex and targeted out-of-plane buckling behaviors, providing a new modular platform that enables the design of the next generation of active and transformable surfaces.

Supplementary videos

Supplementary videos can be found in https://git.fer.me/inclined-metamaterials/videos.

Declaration of competing interest

The authors declare that they have no known competing financial interests or personal relationships that could have appeared to influence the work reported in this paper.

Data availability statement

The data that support the findings of this study are openly available in GitHub at https://git.fer.me/inclined-metamaterials.

Appendix A. Supplementary data

Supplementary material related to this article can be found online at https://doi.org/10.1016/j.eml.2021.101549.

References

[1] P.M. Reis, A perspective on the revival of structural (in) stability with novel opportunities for function: from buckliphobia to buckliphilia, J. Appl. Mech. 82 (11) (2015).

[2] K. Bertoldi, V. Vitelli, J. Christensen, M. Van Hecke, Flexible mechanical metamaterials, Nat. Rev. Mater. 2 (11) (2017) 1–11.

[3] D.M. Kochmann, K. Bertoldi, Exploiting microstructural instabilities in solids and structures: from metamaterials to structural transitions, Appl. Mech. Rev. 69 (5) (2017).

[4] A. Rafsanjani, D. Pasini, Bistable auxetic mechanical metamaterials inspired by ancient geometric motifs, Extrem. Mech. Lett. 9 (2016) 291–296.

[5] T. Mullin, S. Deschanel, K. Bertoldi, M.C. Boyce, Pattern transformation triggered by deformation, Phys. Rev. Lett. 99 (8) (2007) 084301.

[6] K. Bertoldi, M.C. Boyce, S. Deschanel, S. Prange, T. Mullin, Mechanics of deformation-triggered pattern transformations and superelastic behavior in periodic elastomeric structures, J. Mech. Phys. Solids 56 (8) (2008) 2642–2668.

[7] Y. Zhang, E.A. Matsumoto, A. Peter, P.-C. Lin, R.D. Kamien, S. Yang, One-step nanoscale assembly of complex structures via harnessing of an elastic instability, Nano Lett. 8 (4) (2008) 1192–1196.

[8] K. Bertoldi, P.M. Reis, S. Willshaw, T. Mullin, Negative Poisson's ratio behavior induced by an elastic instability, Adv. Mater. 22 (3) (2010) 361–366.

[9] J. Liu, T. Gu, S. Shan, S.H. Kang, J.C. Weaver, K. Bertoldi, Harnessing buckling to design architected materials that exhibit effective negative swelling, Adv. Mater. 28 (31) (2016) 6619–6624.

[10] K. Bertoldi, M.C. Boyce, Mechanically triggered transformations of phononic band gaps in periodic elastomeric structures, Phys. Rev. B 77 (2008) 052105.

[11] P. Wang, F. Casadei, S. Shan, J.C. Weaver, K. Bertoldi, Harnessing buckling to design tunable locally resonant acoustic metamaterials, Phys. Rev. Lett. 113 (1) (2014) 014301.

[12] S. Shan, S.H. Kang, P. Wang, C. Qu, S. Shian, E.R. Chen, K. Bertoldi, Harnessing multiple folding mechanisms in soft periodic structures for tunable control of elastic waves, Adv. Funct. Mater. 24 (31) (2014) 4935–4942.

[13] D. Krishnan, H. Johnson, Optical properties of two-dimensional polymer photonic crystals after deformation-induced pattern transformations, J. Mech. Phys. Solids 57 (9) (2009) 1500–1513.

[14] J. Li, J. Shim, J. Deng, J.T. Overvelde, X. Zhu, K. Bertoldi, S. Yang, Switching periodic membranes via pattern transformation and shape memory effect, Soft Matter 8 (40) (2012) 10322–10328.

[15] D. Yang, B. Mosadegh, A. Ainla, B. Lee, F. Khashai, Z. Suo, K. Bertoldi, G.M. Whitesides, Buckling of elastomeric beams enables actuation of soft machines, Adv. Mater. 27 (41) (2015) 6323–6327.

[16] S. Yang, K. Khare, P.-C. Lin, Harnessing surface wrinkle patterns in soft matter, Adv. Funct. Mater. 20 (16) (2010) 2550–2564.

[17] N. Bowden, S. Brittain, A.G. Evans, J.W. Hutchinson, G.M. Whitesides, Spontaneous formation of ordered structures in thin films of metals supported on an elastomeric polymer, Nature 393 (6681) (1998) 146–149.

[18] S. Wagner, S.P. Lacour, J. Jones, I.H. Pai-hui, J.C. Sturm, T. Li, Z. Suo, Electronic skin: architecture and components, Physica E 25 (2–3) (2004) 326–334.

[19] D.-Y. Khang, H. Jiang, Y. Huang, J.A. Rogers, A stretchable form of single-crystal silicon for high-performance electronics on rubber substrates, Science 311 (5758) (2006) 208–212.

[20] C. Harrison, C.M. Stafford, W. Zhang, A. Karim, Sinusoidal phase grating created by a tunably buckled surface, Appl. Phys. Lett. 85 (18) (2004) 4016–4018.

[21] P.-C. Lin, S. Vajpayee, A. Jagota, C.-Y. Hui, S. Yang, Mechanically tunable dry adhesive from wrinkled elastomers, Soft Matter 4 (9) (2008) 1830–1835.

[22] K. Khare, J. Zhou, S. Yang, Tunable open-channel microfluidics on soft poly (dimethylsiloxane)(PDMS) substrates with sinusoidal grooves, Langmuir 25 (21) (2009) 12794–12799.

[23] Y. Zhang, Z. Yan, K. Nan, D. Xiao, Y. Liu, H. Luan, H. Fu, X. Wang, Q. Yang, J. Wang, et al., A mechanically driven form of Kirigami as a route to 3D mesostructures in micro/nanomembranes, Proc. Natl. Acad. Sci. 112 (38) (2015) 11757–11764.

[24] Z. Yan, F. Zhang, J. Wang, F. Liu, X. Guo, K. Nan, Q. Lin, M. Gao, D. Xiao, Y. Shi, et al., Controlled mechanical buckling for origami-inspired construction of 3D microstructures in advanced materials, Adv. Funct. Mater. 26 (16) (2016) 2629–2639.

[25] R.M. Neville, F. Scarpa, A. Pirrera, Shape morphing Kirigami mechanical metamaterials, Sci. Rep. 6 (1) (2016) 1–12.

[26] C. Ahn, X. Liang, S. Cai, Bioinspired design of light-powered crawling, squeezing, and jumping untethered soft robot, Adv. Mater. Technol. 4 (7) (2019) 1900185.

[27] A. Rafsanjani, Y. Zhang, B. Liu, S.M. Rubinstein, K. Bertoldi, Kirigami skins make a simple soft actuator crawl, Science Robotics 3 (15) (2018).

[28] Y. Yang, Z. You, 3D construction of a tilted cuboid mechanical metamaterial, in: ASME 2018 International Mechanical Engineering Congress and Exposition, American Society of Mechanical Engineers Digital Collection, 2018, pp. 1–8.

[29] D. Chandra, S. Yang, P.-C. Lin, Strain responsive concave and convex microlens arrays, Appl. Phys. Lett. 91 (25) (2007) 251912.

[30] P. Kim, Y. Hu, J. Alvarenga, M. Kolle, Z. Suo, J. Aizenberg, Rational design of mechano-responsive optical materials by fine tuning the evolution of strain-dependent wrinkling patterns, Adv. Opt. Mater. 1 (5) (2013) 381–388.

[31] J. Shim, S. Shan, A. Košmrlj, S.H. Kang, E.R. Chen, J.C. Weaver, K. Bertoldi, Harnessing instabilities for design of soft reconfigurable auxetic/chiral materials, Soft Matter 9 (34) (2013) 8198–8202.

Supplementary Information: Surface Texture Modulation via Buckling in Porous Inclined Mechanical Metamaterials

MATHEUS C. FERNANDES[1,2,†], SAURABH MHATRE[3,†], ANTONIO E. FORTE[1,4,5], BING ZHAO[1,6], OLGA MESA[3,7], JAMES C. WEAVER[1,2], MARTIN BECHTHOLD[3], AND KATIA BERTOLDI[1,2,*]

[1] John A. Paulson School of Engineering and Applied Sciences – Harvard University, Cambridge, MA 02138
[2] Wyss Institute – Harvard University, Cambridge, MA 02138
[3] Graduate School of Design – Harvard University, Cambridge, MA 02138
[4] Department of Electronics, Information and Bioengineering – Politecnico di Milano, Milan, 20133 Italy
[5] Department of Engineering, King's College London, London, WC2R 2LS, UK
[6] Space Structures Research Center, Shanghai Jiao Tong University, Shanghai 200240, China
[7] School of Architecture – Roger Williams University, Bristol, RI 02809
[†] Equal contribution authors
[*] Corresponding author: bertoldi@seas.harvard.edu

S1. GEOMETRY

Conceptually, our metamaterial is generated from slicing a block, containing a square array of cylindrical holes, at an angle θ (fig. S1). The cylindrical holes have radius $R_h = 5.83$ mm and center-to-center distance $d_h = 13.41$ mm, such that the porosity of the structure in the undeformed configuration is $\phi_0 = \pi R_h^2 / d_h^2 = 0.59$. The resulting metamaterial has an out-of-plane thickness $T = 23.32$ mm and elliptical holes on its top and bottom faces with major and minor axis of length $R_h / \cos\theta$ and R_h, respectively.

In this study, we consider finite size samples comprising an array of 6×6 holes in the center, flanked by a column of half holes on all sides to alleviate boundary effects. These samples have size $X_f \times X_f / \cos\theta \times T$, where $X_f = 7 d_h = 93.78$ mm.

Our metamaterial is activated through hydraulic or pneumatic actuation, and as such, the samples were made water/air-tight by covering their top and bottom faces with a thin elastomeric layer (with thickness of $T_{layer} \sim 0.5$ mm). A single pressure input actuation was achieved by connecting the cylindrical cavities together via a series of rectangular channels. The channels are shown in fig. S1 and have a height $H_c = 4.5$ mm, and in the final molded form, had a width of 2 mm.
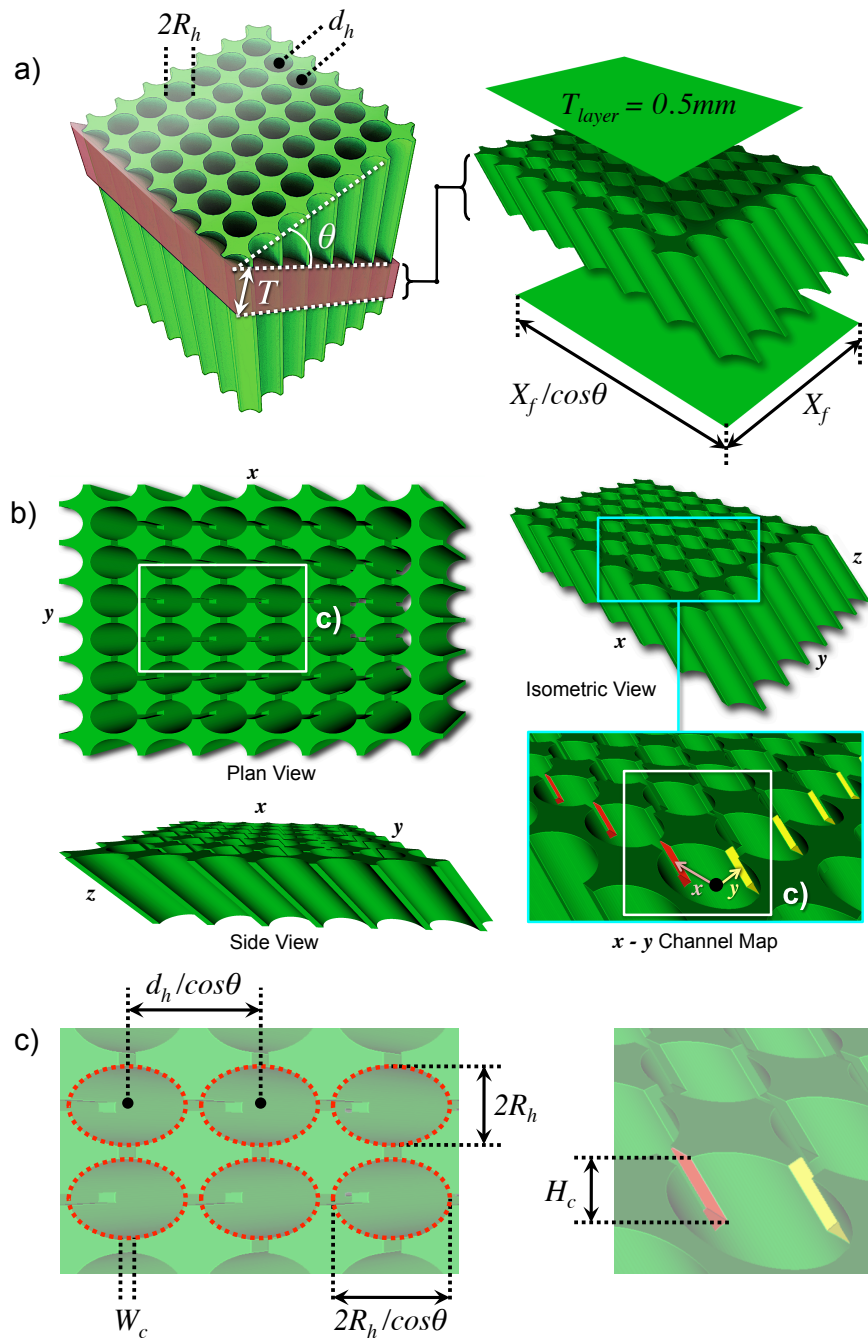
Figure S1: Design elements of our inclined metamaterial. (a) Shows the inclined cut of our metamaterial from a square block of elastomeric matrix and its respective dimensions. On right is the exploded view of the assembly that includes the cut metamaterial and the films with its respective dimensions. (b) Shows the construction of the channel that are located along the top and bottom surfaces of the matamaterial. (c) Outlines the dimensions of the cut metamaterials in addition to the dimensions necessary to reconstruct the experimental sample.

S2. FABRICATION

To fabricate the samples, we first produced molds using a Stratasys Objet30 3D printer from VeroBlue (RGD840) material (fig. S2(a)). Before casting, releasing agent (Easy Release 200, Smooth-On, Inc.) was sprayed on the mold surfaces to further facilitate the de-molding process, and the samples were then cast using a silicone elastomer material (Zhermack Elite Double 32) (fig. S2(b)). Once the silicon elastomer was poured, the mold was quickly placed in a degassing chamber (vacuum chamber) for approximately 8 minutes. This process ensured that any remaining air was removed from the elastomer material prior to curing. Once the degassing process was completed, the cast mixture was allowed to cure at room temperature and atmospheric pressure for approximately four hours. After de-molding the planar structure (fig. S2(c)), two thin sheets were fabricated using the same silicone elastomer material by pouring the uncured rubber onto an inclined acrylic sheet (fig. S2(d)). The sheets were left to cure for 4 hours. Once cured, the thin sheets, each measuring 0.5mm in thickness were glued to the top and bottom surface of the metamaterial using the same silicone elastomer (fig. S2(e)). In fig. S2(f) the channels and the thin sheet are visible. The same gluing process was also used to attach the two molded halves of the metamaterial to each other (fig. S2(g and h)). As a final step, tubes were punctured into the center of the ends (the short edge) of the planar structure and sealed with the same silicone elastomer (fig. S2(i)). The final assembly was left to cure and seal for an additional 4 hours.
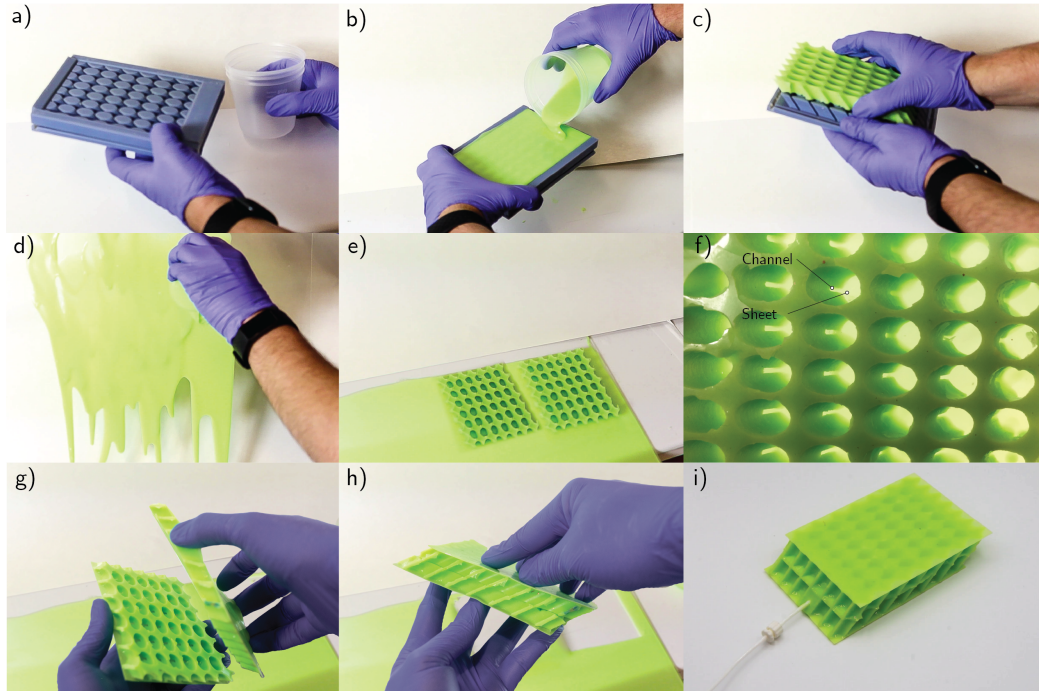
Figure S2: Metamaterial fabrication. (a) The elastomer mixing cup and 3D-printed mold used for creating the sample. (b) Uncured elastomer is poured into the mold. (c) After allowing the elastomer to fully cure, the sample is removed from the mold. (d) Uncured elastomer is evenly poured on top of an acrylic sheet to create a thin film to be used as top and bottom sheets. (e) Two de-molded components are placed with channels face down on top of the cured thin sheet. (f) The thin sheets are glued to the samples using the same uncured silicone elastomer that was used for the other stages of the casting process. (g) The two structures are aligned, and (h) the two structures are glued together with the same elastomer. (i) A tube is punctured into the short edge and sealed with the same elastomer.

S3. EXPERIMENTS

S3.1. Pressure-Volume Curve

To obtain the pressure-volume data, the test specimens were filled with water, while ensuring that all of the air was removed from its internal cavities. Once each specimen was filled, a volume-controlled syringe pump (Standard Infuse/Withdraw PHD Ultra Syringe Pump by Harvard Apparatus) was used to withdraw the fluid from the cavities while a pressure sensor (MPX5050DP, NXP USA Inc.) attached to the withdrawal line measured the pressure inside the sample cavities. The withdrawal process was performed slowly, at 100 ml/min, to ensure the pressure reading obtained on the vacuum line corresponded to the pressure inside of the cavities – avoiding any viscous constrictions from the fluid flow in the tube connecting to the sample.

S3.2. Measuring out-of-plane displacement

To measure the out-of-plane deformation of each structure, the specimen was painted white with spray chalk to minimize the reflective index of its surface, and a hand-held 3D scanner (Artec Space Spider, Artec Studio 14.1.1.75) was used to obtain the full deformation profile of the structure (fig. S3(a)-(b)). Once the scan was obtained (fig. S3(c)), a Python script was used to detect the out-of-plane deformation magnitude at the center of each structure in order to capture the deformation, while avoiding edge effects. The center of the structure was divided into four regions, with each region being sampled independently to measure the deformations around the different adjacent hole locations. In each region, we measured δ by taking the highest z-point on the face and subtracting the lowest z-point on the face, namely $\delta = \max(u_z) - \min(u_z)$.
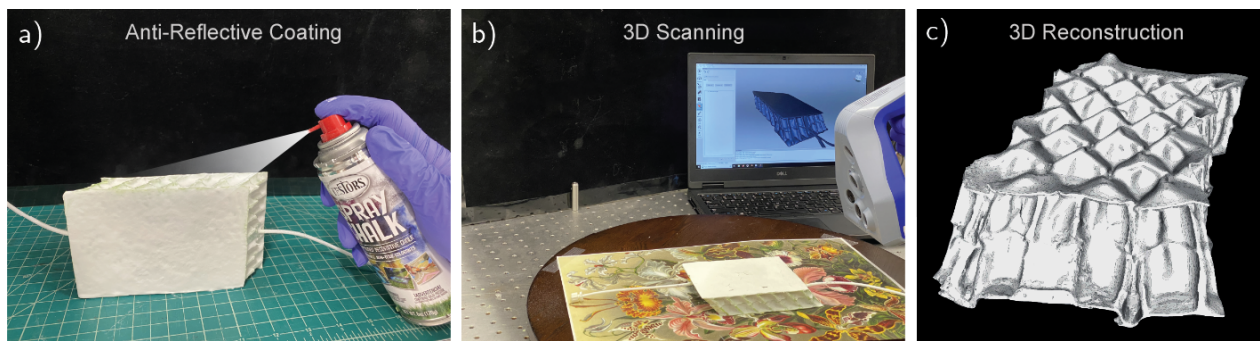

Figure S3: Out-of-plane displacement-3D reconstructions. (a) The elastomeric sample was coated with white spray chalk to give it a non-reflective surface. (b) A 3D scanner (Artec Space Spider) was used to obtain the full deformation profile of the structure. (c) 3D computer model of the structure after post-processing.

S3.3. Light Reflection Experiments

To understand how these structures could be employed to control light reflection, we created a simple experimental setup that captured the specular light reflection from the surface of the $\theta = 0°$ and $\theta = 45°$

samples onto a vertical projection screen. In this setup, we placed each of the specimens in the center of a dark room and projected a goose-neck halogen light at a 45° angle from the surface of the specimen at a distance of 9.5 cm behind the sample. A black wall, located 9.5 cm in front of the sample, contained an attached letter-sized screen onto which the specular reflection pattern from the sample was projected (as shown in fig. 3 of the main manuscript). A video camera was placed perpendicular to the screen and recorded the projected reflection pattern. As water was removed from the holes using the syringe pump, the reflection pattern was captured by the camera. The pattern information collected by the camera was then post-processed using a custom Python script. In this code, each frame was processed independently by systematically converting the color scale into gray scale. For each frame, the directional mean reflectance, R_Ω, was measured by averaging the brightness of all gray scale pixels contained on the pattern collection screen.

S4. NUMERICAL SIMULATIONS

S4.1. Finite Element Simulations

The finite element analyses presented in this article were conducted using *ABAQUS/Explicit* (SIMULIA, Providence, RI). The model geometry was constructed using solid 8-node linear brick, reduced integration 3D elements (*ABAQUS* element code C3D8R) for the porous metamaterial. The top and bottom films used to seal the porous metmaterial were meshed using 4-node doubly curved thin shell elements with reduced integration (*ABAQUS* element code S4R). It is important to note that in these models, we did not incorporate the geometry of the channels as we defined a fluid filled cavity model comprising all of the holes. Actuation of the models was achieved by shrinking the volume of the fluid filled cavity. In all our simulations, the response of the elastomeric material was captured using an incompressible Neo-Hookean material model with normalized shear modulus μ.

In fig. S4 we present numerical snapshots for five different hole arrangements: (*i*) square array; (*ii*) triangular array; (*iii*) hexagonal array; (*iv*) rhombitrihexagonal array; (*v*) trihexagonal array. In full agreement with previous studies[1], we found that when the holes' axes are perpendicular to the top and bottom surfaces (i.e. $\theta = 0$), buckling triggers a planar geometric transformation. For $\theta = 45°$, all geometries exhibited different buckling-induced out-of-plane deformation patterns. Finally, the numerical results for the metamaterial with a square array of holes closely match the experimental data reported in Fig. 1 of the main text, confirming the validity of our simulations.
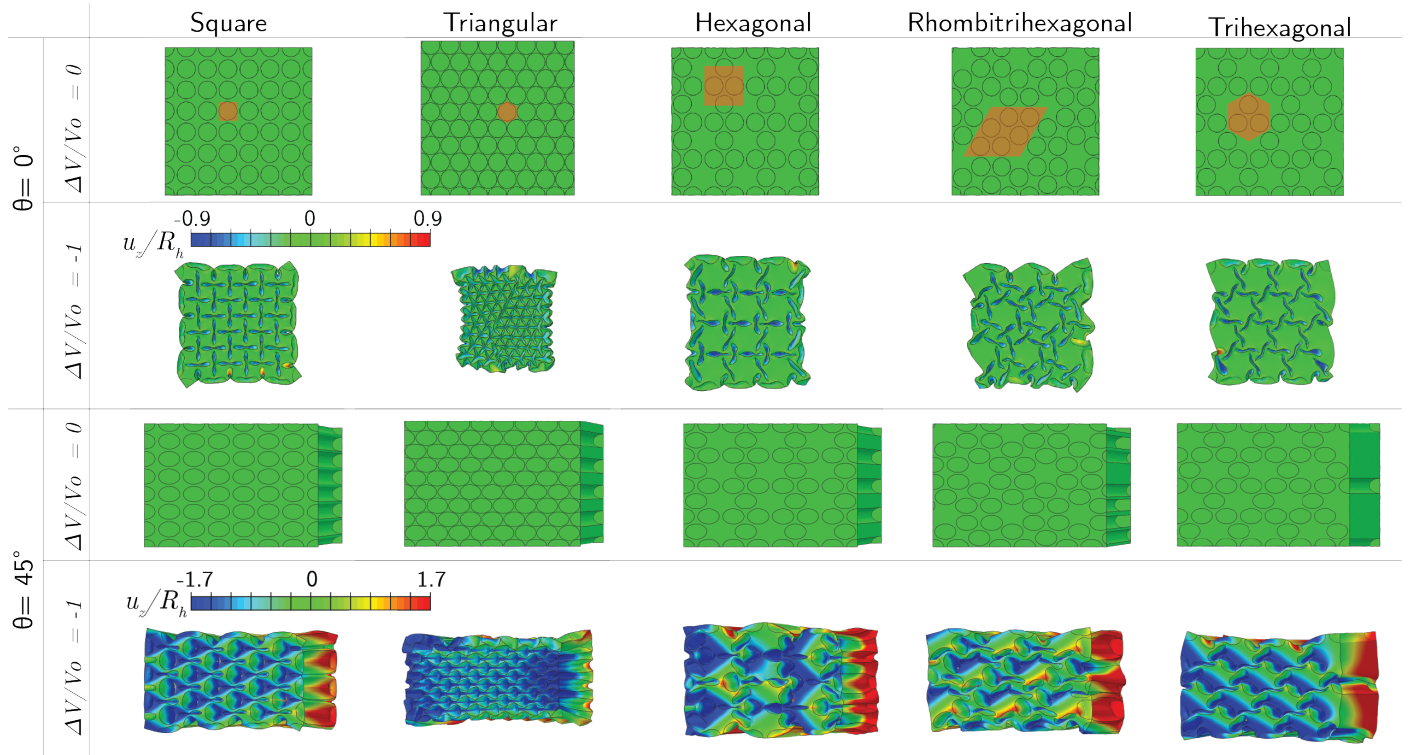
Figure S4: Buckling-induced surface geometries for different hole patterns. Finite Element results for five hole arrangements with $\theta = 0°$ (top) and $\theta = 45°$ (bottom) at $\Delta V/V_0 = 0$ and $\Delta V/V_0 = -1$, for square, triangular, hexagonal, rhombitrihexagonal, and trihexagonal arrays of holes. In the images, we show the normalized out-of-plane displacement, u_z/R_h.

S4.2. Ray Tracing Simulations

To simulate the effect of buckling on light reflection, we conducted ray tracing simulations using the Ray Tracing Module in COMSOL Multiphysics 5.0 (COMSOL Inc., Burlington, MA). To create the COMSOL models, we first exported the deformed meshes from ABAQUS and then boolean subtracted them from a cube with edges approximately three times the length of the metamaterial, X_f. This cube with its subtracted shape of the deformed metamaterial represented the medium in which the rays propagated, to which we assigned a material refractive index of $n = 1$. The domain was meshed using a free tetrahedral mesh and a time-depended solver (Generalized-alpha, backward Euler) was utilized to solve for the time evolution of the ray tip location. In all our simulations, a 9 by 9 array of rays (totaling 81 rays) was initialized on the boundary of the meshed medium and was propagated at a 45° angle from the surface of sample. Furthermore, we defined freeze wall conditions (freezing a ray upon contact) on the outer boundaries of the optics domain to ensure finite time convergence and bounce wall boundary conditions (specular reflection) on the surface of the metamaterial.
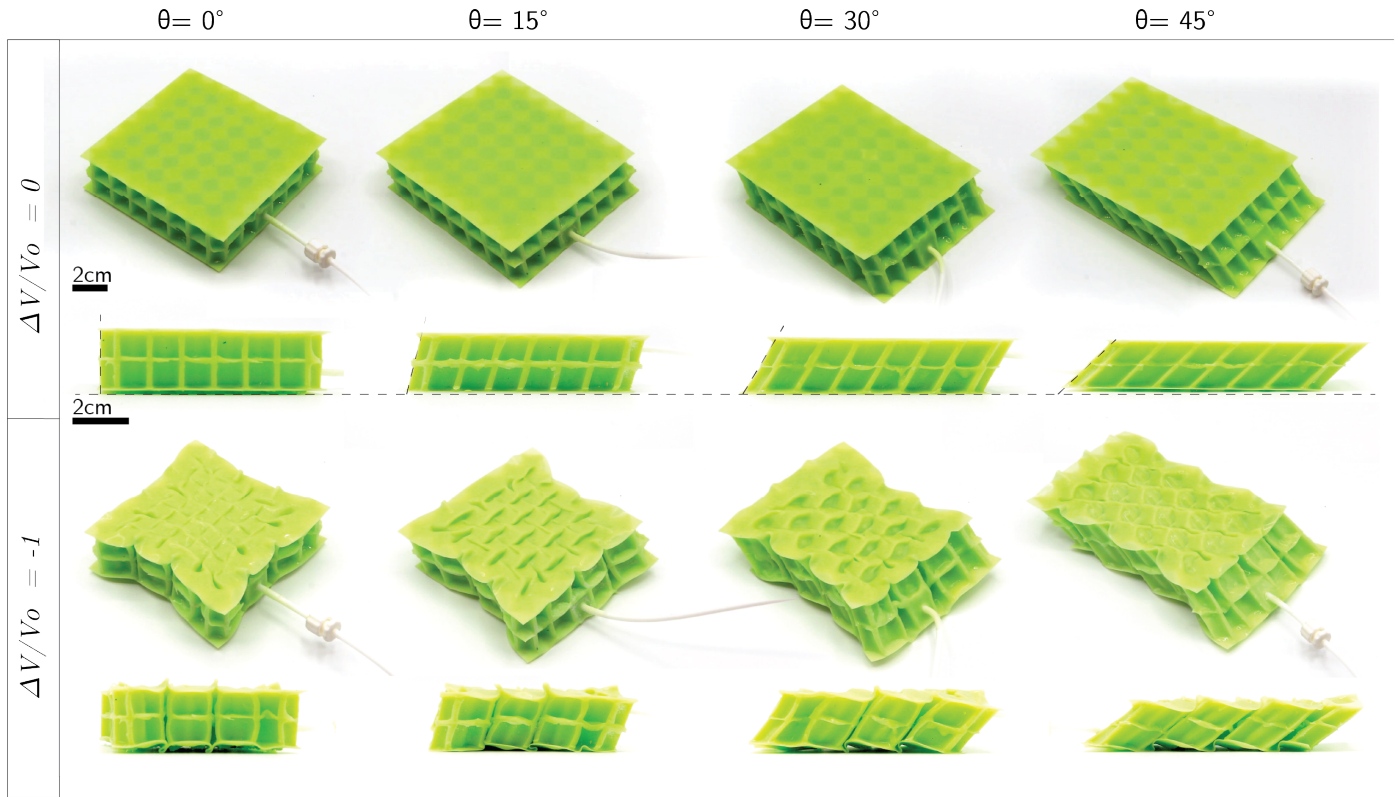
S5. ADDITIONAL RESULTS

Figure S5: Deformation for samples with $\theta = 0°$**,** $15°$**,** $30°$ **and** $45°$**.** Photos of the metamaterial at $\Delta V/V_0 = 0$ (top) and at $\Delta V/V_0 = -1$ configurations for samples with $\theta = 0°$, $15°$, $30°$ and $45°$. Both top and side views are shown.
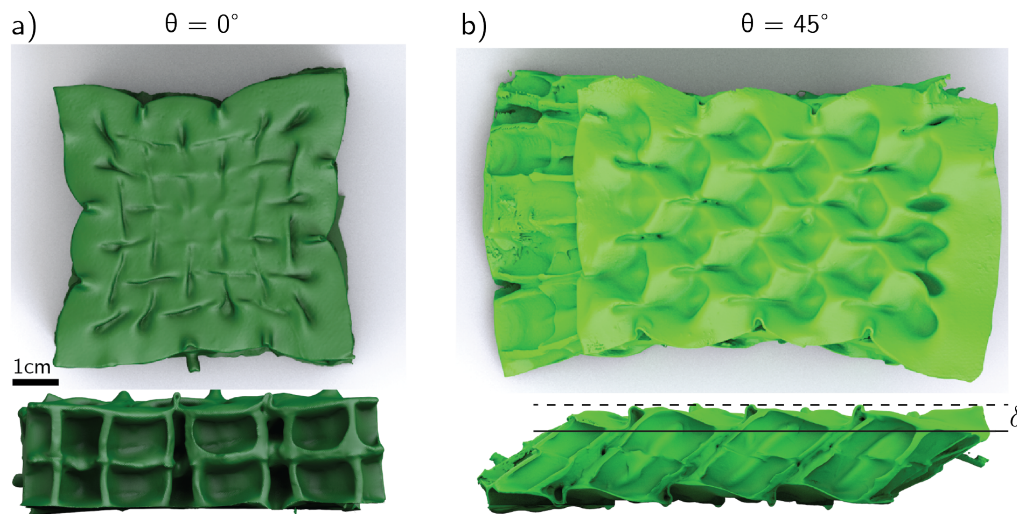

Figure S6: 3D scans of the buckled samples. Top and side view of the scanned profile of samples with (a) $\theta = 0°$ and (b) $\theta = 45°$ at $\Delta V/V_0 = -1$.

a) θ=0° with spheres   **b)** θ=45° with spheres   **c)** θ=45° with plates
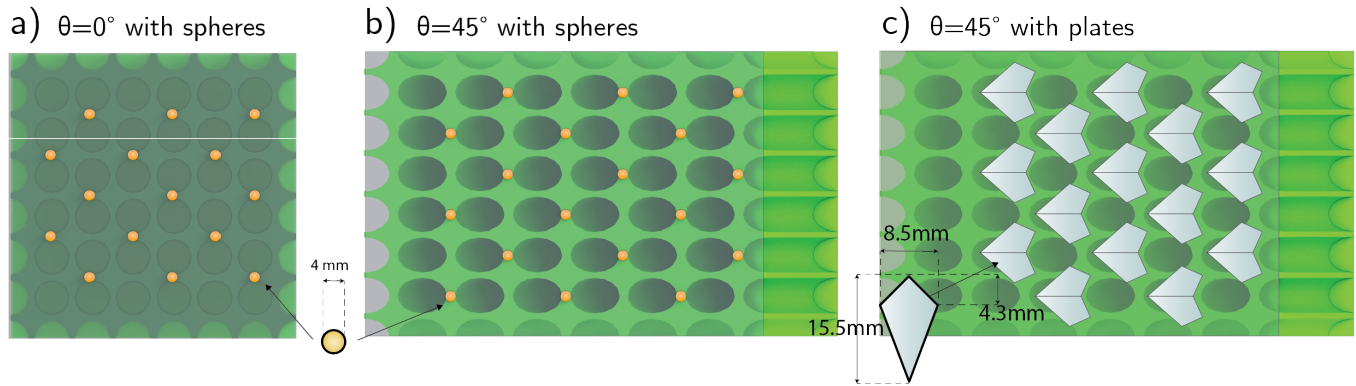

4 mm

8.5mm

15.5mm

4.3mm

Figure S7: Sphere and plate placement. (a) Schematics showing the placement locations of the acrylic spheres on the bottom surface of $\theta = 0°$ sample. In this configuration, the sample always has the same coefficient of friction independent of $\Delta V / V_0$. (b) Schematics showing the placement locations of the acrylic spheres on the bottom surface of $\theta = 45°$ sample. In this configuration, the sample has low friction at $\Delta V / V_0 = 0$ and high friction at $\Delta V / V_0 = -1$. (c) Schematics showing the placement locations of the acrylic plates on the bottom surface of $\theta = 45°$ sample. In this configuration, the sample has high friction at $\Delta V / V_0 = 0$ and low friction at $\Delta V / V_0 = -1$.

a) θ= 0°   **b)** θ= 45°   **c)**
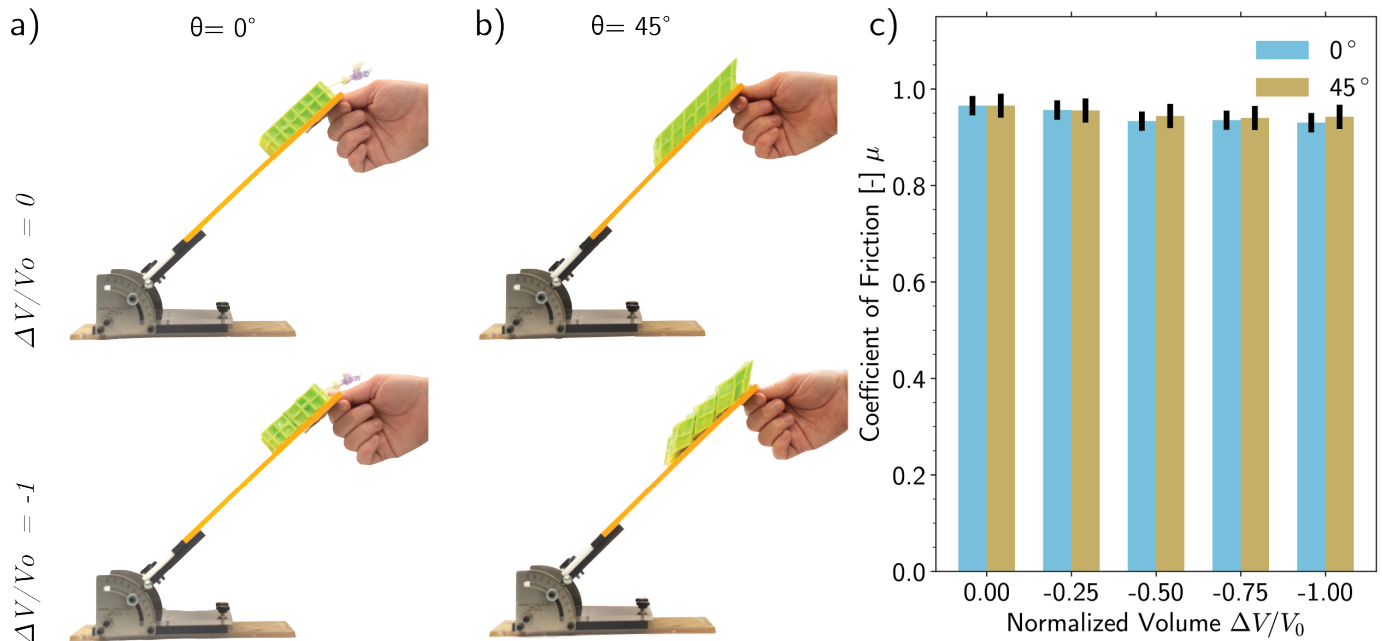
$\Delta V/V_0 = 0$

$\Delta V/V_0 = -1$

Figure S8: Frictional properties of the metamaterial without acrylic features. (a) Photographs qualitatively showing the effect of the buckling-induced morphology on the tilting angle φ_{cr} for which samples with (a) $\theta = 0°$ and (b) $\theta = 45°$ and no acrylic feature attached to their bottom surface, began to slide. We find that for both samples, φ_{cr} is not affected by ΔV. (c) Coefficient of friction for the two samples as a function of $\Delta V / V0$.

θ=45° with plates

2cm

θ=45° with spheres

θ=45°

θ=0° with spheres

θ=0°

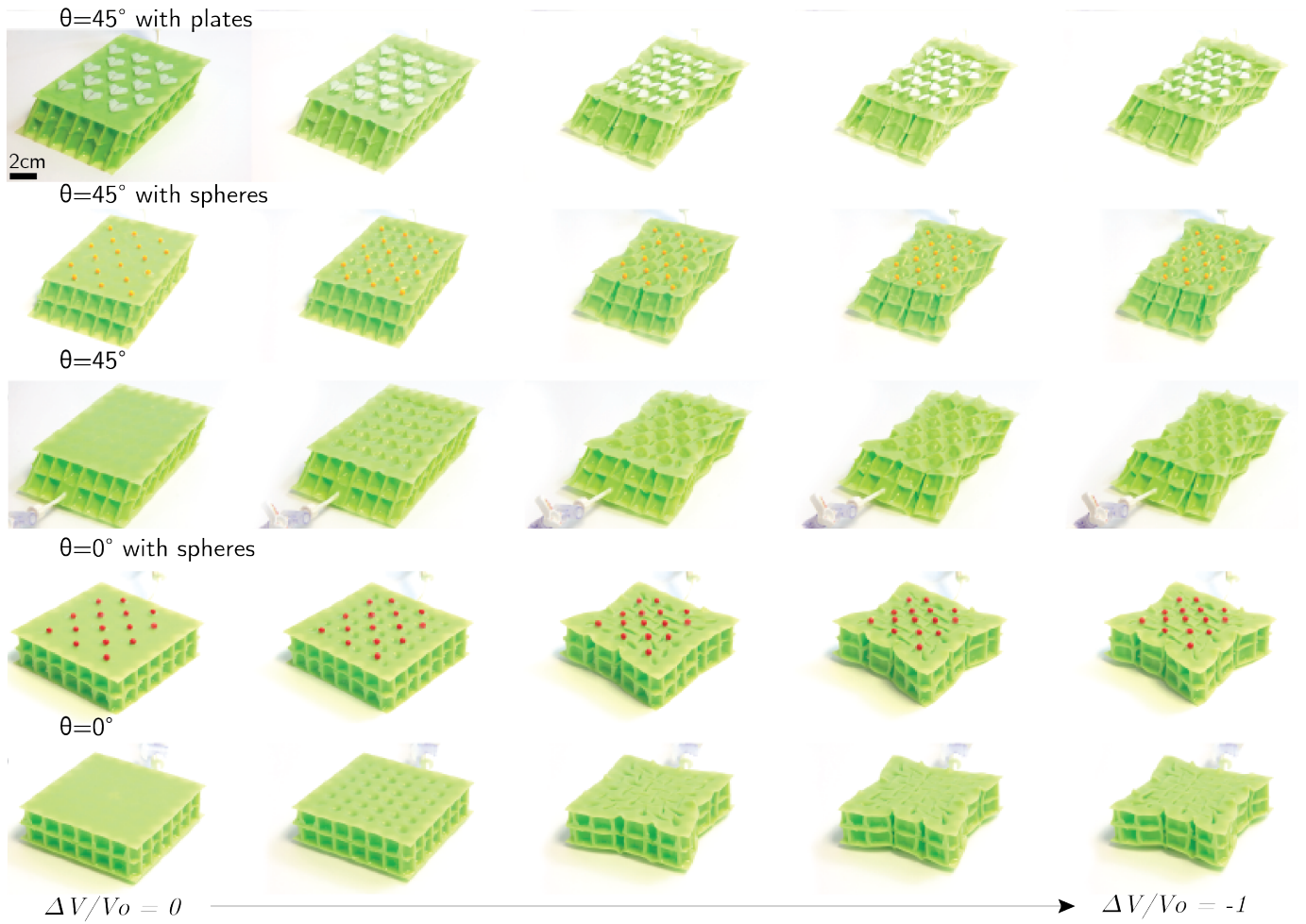$\Delta V/Vo = 0$ ────────────────────────────────► $\Delta V/Vo = -1$

Figure S9: Deformation for samples with acrylic features attached to their surface. Photos at decreasing values of $\Delta V/V_0$ of the metamaterials with (*i*) $\theta = 45°$ and acrylic plates; (*ii*) $\theta = 45°$ and acrylic spheres; (*iii*) $\theta = 45°$ and no acrylic features; (*iv*) $\theta = 0°$ and acrylic spheres; (*v*) $\theta = 0°$ and no acrylic features.
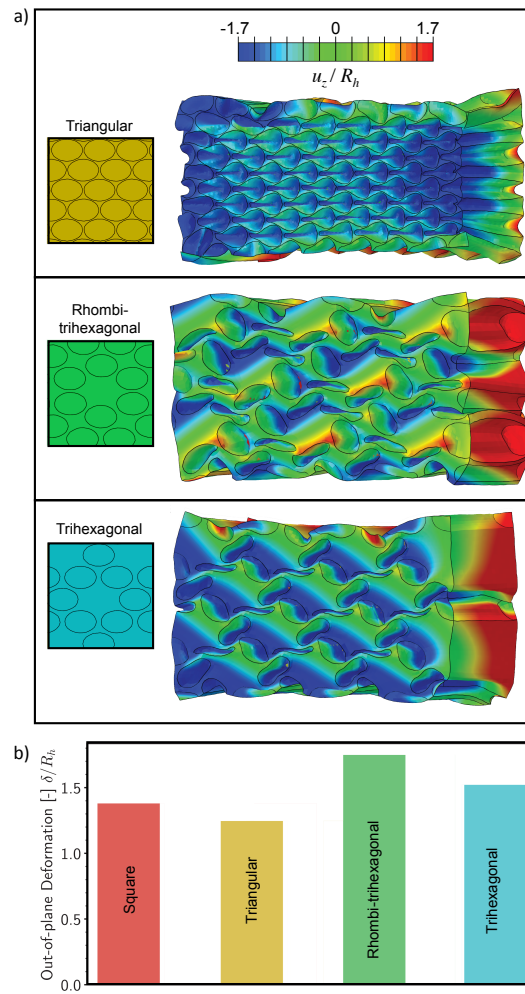
Figure S10: Out-of-plane buckling behaviors for different hole patterns. Post-buckling Finite Element results for three hole arrangements with $\theta = 45°$ at $\Delta V / V_0 = -1$. For the triangular, rhombitrihexagonal, and trihexagonal holes arrays (the undeformed geometry is shown in the insets), we illustrate the normalized out-of-plane displacement, u_z / R_h. (b) Normalized out-of-plane deformation measurements obtained from Finite Element simulations at $\Delta V / V_0 = -1$ for the triangular, rhombitrihexagonal, and trihexagonal geometries, and the square arrangement from **??**. Additional information on this figure can be found in Supplementary Video 6.

REFERENCES

[1] Shim, J., Shan, S., Košmrlj, A., Kang, S. H., Chen, E. R., Weaver, J. C., and Bertoldi, K. (2013). Harnessing instabilities for design of soft reconfigurable auxetic/chiral materials. *Soft Matter*, 9(34):8198–8202.